J. Fluid Mech. (2024), *vol*. 980, A38, doi:10.1017/jfm.2024.41

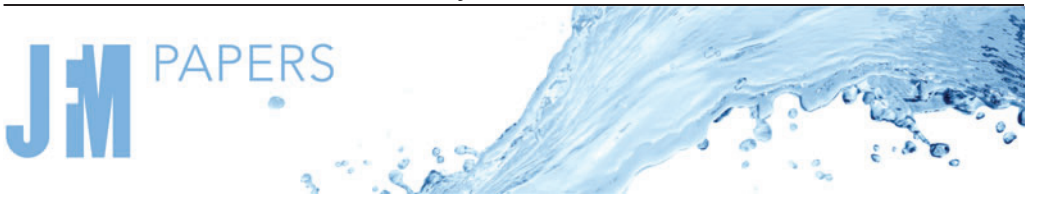

Preferential accumulation of finite-size particles in near-wall streaks

Cheng Peng[1],†, **Lian-Ping Wang**[2,3] **and Songying Chen**[1]

[1]Key Laboratory of High Efficiency and Clean Mechanical Manufacture, Ministry of Education, School of Mechanical Engineering, Shandong University, Jinan 250061, PR China

[2]Guangdong Provincial Key Laboratory of Turbulence Research and Applications, Center for Complex Flows and Soft Matter Research and Department of Mechanics and Aerospace Engineering, Southern University of Science and Technology, Shenzhen, Guangdong 518055, PR China

[3]Guangdong-Hong Kong-Macao Joint Laboratory for Data-Driven Fluid Mechanics and Engineering Applications, Southern University of Science and Technology, Shenzhen, Guangdong 518055, PR China

(Received 18 September 2023; revised 17 December 2023; accepted 7 January 2024)

The preference for particles to accumulate at specific regions in the near-wall part is a widely observed phenomenon in wall-bounded turbulence. Unlike small particles more frequently found in low-speed streaks, finite-size particles can accumulate in either low-speed or high-speed streaks. However, mechanisms and influencing factors leading to the different preferential concentration locations still need to be clarified. The present study conducts particle-resolved direct numerical simulations of particle-laden turbulent channel flows to provide a better understanding of this seemingly puzzling behaviour of preferential accumulation. These simulations cover different particle-to-fluid density ratios, particle volume fractions, particle sizes and degrees of sedimentation intensity. We find that the large particle size is the crucial factor that results in particles accumulating in high-speed streaks. Large particles not only are difficult to be conveyed by the quasi-streamwise vortices to low-speed streaks but also can escape from the near-wall region before moving spanwisely out from high-speed streaks. The sedimentation effect allows particles to gather closer to the channel wall and stay longer in the near-wall regions, reinforcing the sweeping mechanism of quasi-streamwise vortices that transport particles from high- to low-speed streaks. As a result, sedimenting particles tend to accumulate in the low-speed streaks.

Key words: particle/fluid flow

† Email address for correspondence: pengcheng@sdu.edu.cn

1. Introduction

Quasi-streamwise vortices dominate the near-wall flow structures of wall-bounded turbulent flows. These quasi-streamwise vortices could bring high-speed fluids outside the viscous sublayer to the near-wall region and take low-speed fluids away from the near-wall region. As a result, the instantaneous distribution of the streamwise fluid velocity on a near-wall plane parallel to the wall would exhibit low-speed streaks (LSS) and high-speed streaks (HSS) appearing alternately. When particles are present, they preferentially accumulate in LSS or HSS. In some studies, this phenomenon was called 'preferential concentration'. To differentiate from the preferential concentration of particles in the low-vorticity and high-strain-rate regions (Maxey 1987; Squires & Eaton 1990; Wang & Maxey 1993), we term the preference of particles to sample in LSS or HSS 'preferential accumulation' (PA) in the rest of this study.

Preferential accumulation is one of the most well-known results of the dynamic interaction of particles with the coherent structures of near-wall turbulence. It was widely observed in both experiments (e.g. Rashidi, Hetsroni & Banerjee 1990; Niño & Garcia 1996; Suzuki, Ikenoya & Kasagi 2000; Fong, Amili & Coletti 2019; Berk & Coletti 2023) and numerical simulations (e.g. Pedinotti, Mariotti & Banerjee 1992; Marchioli & Soldati 2002; Kidanemariam *et al.* 2013; Zhu *et al.* 2020) with a wide range of flow and particle parameters. Unlike the numerical simulations that could directly show particles non-uniformly distributed among near-wall streaks, some experiments inferred the existence of PA in LSS from the particle streaks that move slower than the averaged fluid velocity. Preferential accumulation is also not limited to spherical particles, as similar phenomena were reported in studies with spheroidal particles (Eshghinejadfard, Zhao & Thévenin 2018), or even fibres (Marchioli, Fantoni & Soldati 2010; Do-Quang *et al.* 2014).

For a long time, PA in LSS was almost exclusively observed in a series of studies. Pedinotti *et al.* (1992) reported their Lagrangian point-particle simulations in a horizontal open-channel flow and found that particles with intermediate inertia $\tau_p^+ \equiv \tau_p u_\tau / y_\tau \approx 3$, where τ_p is the particle response time, and the superscript '+' indicates normalization by the friction velocity u_τ and the wall unit y_τ, were more likely to sample in LSS, whereas particles with greater ($\tau_p^+ \approx 8$) or lesser ($\tau_p^+ \approx 0.32$ and 1.0) inertia distributed more uniformly in the near-wall regions. Pan & Banerjee (1996) studied the particle size effect on PA of almost neutrally buoyant particles. They concluded that larger particles ($d_p^+ \equiv d_p / y_\tau = 2$ and 4, where d_p is the particle diameter) yielded more predominate PA in LSS than smaller particles ($d_p^+ = 1$). Niño & Garcia (1996) experimentally investigated the particle distribution in horizontal turbulent channel flows. They found particles with sizes smaller than the thickness of the viscous sublayer (typically $y^+ \leq 8$, where y is the wall-normal distance from the wall) to accumulate in LSS. However, PA in LSS was preserved even when τ_p^+ was down to 0.04, which was way below the lower bound of τ_p^+ reported by Pedinotti *et al.* (1992), under which a nearly uniform distribution of particles was to be expected. Niño & Garcia (1996) also reported the disappearance of PA when the particle size exceeded the thickness of the viscous sublayer and $\tau_p^+ > 10$, which was consistent with the observation in Pedinotti *et al.* (1992). Marchioli & Soldati (2002) observed PA in LSS in upward vertical channel turbulence with point-particle simulations. Unlike the previously mentioned studies, that study did not include the sedimentation effect along the wall-normal direction, and the particle-to-fluid density ratio was as high as 769, which resulted in τ_p^+ ranging up to 116.3, way above the upper limit of $\tau_p^+ = 10$ in the study of Niño & Garcia (1996). Fong *et al.* (2019) reported a similar observation of PA in LSS in their experimental measurements of gas–solid flow with τ_p^+ ranging from 70

to 140. We also note that both Marchioli & Soldati (2002) and Fong *et al.* (2019) achieved large τ_p^+ by adopting large particle-to-fluid density ratios (particle sizes were still small), whereas in earlier works of Pedinotti *et al.* (1992) and Niño & Garcia (1996) where PA disappeared when $\tau_p^+ \gtrapprox 10$, it was the particle size that was enlarged, i.e. $d_p^+ = 1.29$–11.8 and 4.3–7.7 in the latter two studies, compared with $d_p^+ = 0.3$–1.65 and 0.78–1.1 in the former ones, respectively. This difference may imply that PA depends separately on the particle size and density ratio rather than their combined property of particle inertia.

In recent years, particle-resolved direct numerical simulations (PR-DNS) were also used to investigate the particle–fluid interactions in wall-bounded turbulence. Some of these investigations reported PA of particles in near-wall streaks. Shao, Wu & Yu (2012) conducted PR-DNS of large particles in fully developed turbulent channel flows. Particles in that study were quite large, $d_p^+ = 21$ and 42, resulting in τ_p^+ of 37 and 147. The PA of sediment particles in low-speed regions was observed near the bottom wall. Notably, although the particle volume fractions in that study were relatively large (up to 7 %), and the presence of particles significantly modulated the near-wall streaks, we still term the phenomenon PA in LSS for convenience of discussion. Another notable phenomenon reported in this study was that particles could also overly sample in high-speed fluids near the top channel wall under a weak sedimentation effect. Through PR-DNS, Kidanemariam *et al.* (2013) showed PA in LSS for particles with $d_p^+ = 7.21$ and $\tau_p^+ = 4.9$. These selected particle parameters did not exceed the upper limit reported by Niño & Garcia (1996), beyond which the PA would disappear. Pestana, Uhlmann & Kawahara (2020) investigated the motion of finite-size particles in an idealized fluid field combining the equilibrium solution and coherent vortex structures in turbulent plane Couette flows. Under the drifting of quasi-streamwise vortices, particles migrated to low-speed regions. More recently, Xia *et al.* (2021) and Yang *et al.* (2021) observed PA of finite-size particles in LSS in their PR-DNS of downward turbulent channel flows. The particle sizes in those two studies were $d_p^+ \approx 18.8$ and 30, and the resulting τ_p^+ were 39.3 and 57.5, respectively. Unlike Pedinotti *et al.* (1992) and Niño & Garcia (1996) who observed PA of sediment particles disappearing when d_p^+ exceeded the thickness of the viscous sublayer, the studies of Xia *et al.* (2021) and Yang *et al.* (2021) did not include the sedimentation effect along the wall-normal direction. This contrast implies that the sedimentation effect could play a role in PA.

Mechanisms resulting in PA have also been explored in the literature. The spanwise sweeping induced by the quasi-streamwise vortices was recognized as one of the essential mechanisms for PA in LSS (Niño & Garcia 1996; Shao *et al.* 2012; Kidanemariam *et al.* 2013). As illustrated in figure 1, strong quasi-streamwise vortices that carry particles to the near-wall region would further swipe those particles to LSS. Through careful PR-DNS, Kidanemariam *et al.* (2013) gathered statistical pictures of vortex structures around the preferentially sampled particles, which provided convincing evidence for the causality between the spanwise sweeping of quasi-streamwise vortices and PA in LSS. Marchioli & Soldati (2002) noted the formation of counter-rotating vortices under the strong quasi-streamwise vortices that conveyed particles to the near-wall regions. They argued that those weak vortices would prevent particles from being re-entrained by the ejection events and leave LSS, reinforcing the observation of PA in LSS.

Although the mechanisms mentioned above seem sufficient to explain PA in LSS, some recent PR-DNS studies also reported PA of particles in HSS, which is inconsistent with the mechanisms noted above. The ‘abnormal’ phenomenon of PA in HSS was first observed in fully resolved simulations of finite-size long fibres. Do-Quang *et al.* (2014) found that, unlike line-like fibres that gathered in LSS (Marchioli *et al.* 2010), finite-size

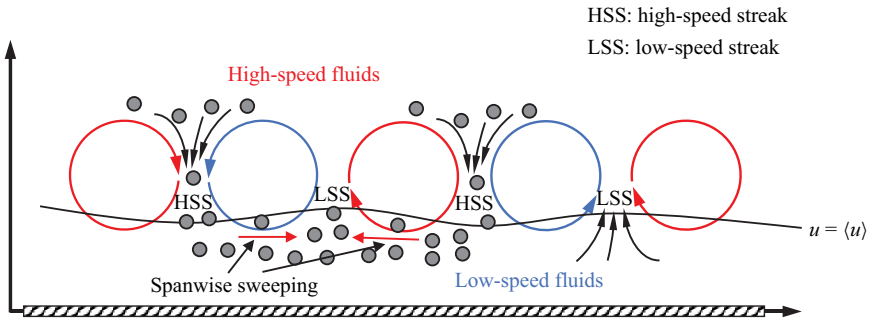

Figure 1. The spanwise sweeping that was viewed as the main mechanism for PA in LSS.

cylindrical fibres appeared more in HSS. They attributed this outlier to the particle–wall interactions that prevent particles from being carried by the spanwise sweeping (Voth & Soldati 2017). Later, Eshghinejadfard *et al.* (2018) also observed PA in HSS with neutrally buoyant spheroid oblates and spherical particles in horizontal channel turbulence. They also explained their observations with particle–wall interactions but did not provide further justifications. Zhu *et al.* (2020) discovered PA of finite-size spherical particles in HSS in upward vertical channel turbulence. They argued that particles in the upward channel moved toward the channel centre under Saffman lift forces (Saffman 1965). These particles could feel the anti-spanwise sweeping induced by the streamwise vortices and move toward the high-speed regions. However, the explanation of Zhu *et al.* (2020) is debatable because the anti-spanwise sweeping happens way above the wall-normal plane where alternate LSS and HSS dominate. According to Moin & Kim (1982) and Moin & Spalart (1987), streak distributions of streamwise fluid velocity were most profound under $y^+ = 10$, while the anti-spanwise sweeping induced by quasi-streamwise vortices occurred most likely between $20 \leq y^+ \leq 35$ (Kim, Moin & Moser 1987). It is noteworthy that in all studies mentioned above reporting PA in HSS, particles are large compared to the wall unit, i.e. $L^+ = 5.12$–38.4 (L is the fibre length) in the study of Do-Quang *et al.* (2014), and $d_p^+ = 27.69$ and 18 in the simulations of Eshghinejadfard *et al.* (2018) and Zhu *et al.* (2020), respectively. This observation indicates that PA in HSS could also result from a particle size effect (but not necessarily due to particle–wall interactions), similar to the disappearance of PA in LSS as observed in Niño & Garcia (1996). Nevertheless, the mechanisms responsible for PA in HSS need more exploration.

The present study is motivated to resolve some of the puzzling observations mentioned above and to provide a reasonable explanation for PA in HSS. We conduct PR-DNS based on the lattice Boltzmann method (LBM) to investigate how the particle-to-fluid density ratio ρ_p/ρ_f, sedimentation effect, particle volume fraction and particle size influence PA and explore the mechanisms for these influences. The remainder of the paper is structured as follows. In § 2, we briefly introduce the simulation set-up and the numerical method to conduct PR-DNS. Since we have already validated the numerical approach in a series of previous PR-DNS studies (Wang *et al.* 2016; Brändle de Motta *et al.* 2019), only limited validations of the particle–wall interactions are presented. The PA phenomena observed in different simulations are discussed in § 3, where the mechanisms resulting in different PA behaviours are also explored. Finally, we recapitulate the main conclusions in § 4. Although turbulence modulation is not our main objective in this study, the flow statistics generated by the present simulations are also provided for future comparisons and benchmarking.

Case	ϕ_p	d_p/h	N_p	ρ_p/ρ_f	Θ	$\nu g/u_\tau^3$	Ga	τ_p^+	$e_{n,d}$	$e_{t,d}$	$\mu_{c,wet}$
A	0.015	0.1605	670	1.0	∞	0	0	46.39	0.97	0.39	0.15
B0	0.015	0.1605	670	2.5	∞	0	0	115.97	0.97	0.39	0.15
B1	0.015	0.1605	670	2.5	0.907	0.0254	30.34	115.97	0.97	0.39	0.15
B1-R-S	0.003	0.0535	3614	2.5	0.907	0.0763	10.11	12.89	0.97	0.39	0.15
B2	0.015	0.1605	670	2.5	0.2	0.1154	64.61	115.97	0.97	0.39	0.15
B2-R	0.003	0.1605	670	2.5	0.2	0.1154	64.61	115.97	0.97	0.39	0.15
C0	0.015	0.1605	670	7.8	∞	0	0	361.83	0.97	0.34	0.02
C1	0.015	0.1605	670	7.8	0.907	0.0056	30.34	361.83	0.97	0.34	0.02
C2	0.015	0.1605	670	7.8	0.2	0.0254	64.61	361.83	0.97	0.34	0.02
C2-R	0.003	0.1605	670	7.8	0.2	0.0254	64.61	361.83	0.97	0.34	0.02

Table 1. Physical parameters of the particles.

2. Parameter setting and simulation details

The present study uses PR-DNS to investigate how particle parameters affect the PA of finite-size particles in near-wall streaks and analyse the corresponding mechanisms. For this purpose, a fully developed turbulent channel flow bounded by two infinite solid walls is used as the geometrical configuration. We choose a confined channel rather than a computationally efficient open channel to bring non-settling particles into discussions since many previous studies involving PA considered either neutrally buoyant particles or particles in vertical channels. The flow is driven by a constant pressure gradient, and the friction Reynolds number when the flow reaches the statistically stationary state is $Re_\tau = u_\tau h/\nu = 180$, where u_τ is the friction velocity, h is the half-channel width and ν is the fluid kinematic viscosity. The boundary condition in the wall-normal direction (y) is no slip, and the boundary conditions in the streamwise and spanwise directions are periodic.

We set up ten PR-DNS cases with mono-dispersed finite-size particles of different parameters, as summarized in table 1. Those cases consider particles with three particle-to-fluid density ratios, i.e. $\rho_p/\rho_f = 1.0$, 2.5, and 7.8 (labelled as Case A, Case B and Case C), which roughly represent neutrally buoyant, glass and steel particles in water. We set those cases mainly to find out how particle inertia affects the PA in the near-wall streaks since previous studies reported quite different observations on the disappearance of PA when the particle inertia became large, i.e. Pedinotti *et al.* (1992) and Niño & Garcia (1996) noted the disappearance of PA when $\tau_p^+ \gtrapprox 10$, whereas Marchioli & Soldati (2002) and Fong *et al.* (2019) still observed PA in HSS when $\tau_p^+ > 70$. As reviewed in the Introduction, these conflicting results in the literature could imply that particle density and size might act differently in affecting PA. Therefore, understanding PA using τ_p^+ alone may not be appropriate.

We also consider three levels of sedimentation effect to find out how gravitational sedimentation affects PA in the near-wall regions. The degree of sedimentation effect is quantified by the Shields number $\Theta = \rho_f u_\tau^2/[g d_p(\rho_p - \rho_f)]$, i.e. non-settling particles with $\Theta = \infty$, weakly settling particles with $\Theta = 0.907$ and strongly settling particles with $\Theta = 0.2$, labelled as '0', '1' and '2', respectively. The Shields number was widely used to quantify the relative importance between shearing and gravitational effects in previous studies of sediment–turbulence interactions (e.g. Shao *et al.* 2012; Kidanemariam *et al.* 2013; Ji *et al.* 2014; Yousefi, Costa & Brandt 2020). Alternatively, one may use the Galileo number $Ga = \sqrt{(\rho_p/\rho_f - 1) g d_p^3}/\nu$ to quantify the intensity of the gravitational effect, the

values of which are also given in table 1. The relationship between Θ and Ga reads $Ga = d_p^+/\sqrt{\Theta}$. Since most cases in the present study have the same particle size, Ga and Θ can be used interchangeably. Compared with the Shields number, Ga measures the relative importance between the gravitational force and viscous drag. In wall-bounded turbulence characterized by strong shearing, the lift forces potentially contribute to the PA of particles in near-wall streaks. This deduction comes from previous studies that reported opposite PA phenomena in upward and downward vertical channel flows, where the sedimentation effect was absent (e.g. Xia *et al.* 2020; Zhu *et al.* 2020; Yang *et al.* 2021).

In most simulated cases, the particle volume fraction ϕ_p is set to 1.5 %. Previous PR-DNS studies considered both higher and lower particle volume fractions, e.g. 5 % in Eshghinejadfard *et al.* (2018), 2.36 % in Shao *et al.* (2012) and 0.05 % in Kidanemariam *et al.* (2013), and PA in the near-wall region was reported. Under strong sedimentation effects, most particles stay close to the bottom wall, which could significantly modify the near-wall coherent structures. To ensure clear near-wall streaks are still being observed, we add two simulations with a reduced particle volume fraction $\phi_p = 0.3$ % for the cases with strong sedimentation effect, namely Cases B2-R and C2-R ('R' means reduced volume fraction) in addition to Cases B2 and C2, respectively. The comparison between cases with different particle volume fractions could also indicate the effect of particle volume fraction on PA. Finally, we also include Case B1-R-S ('S' for smaller particle size) with only one-third of the particle diameter in other cases to study the particle size effect on PA. In this case, the particle volume fraction is set to 0.3 % to reduce the number of particles and the computational costs.

Similar to our previous studies, we adopt the LBM coupled with the interpolated bounce-back (IBB) schemes to handle the no-slip boundary conditions on the particle surfaces. The forces and torques on particles are computed with the momentum-exchange methods, which ensure second-order accuracy for the fluid velocity and fluid–particle interactions. Aside from a series of validation tests in laminar and turbulent flows (Peng 2018), the numerical approach has been cross-examined by comparing with some other alternative methods for turbulent dispersed flows, such as LBM-based immersed boundary method (Peng *et al.* 2019*a*), finite-volume-based direct-forcing fictitious-domain method (Wang *et al.* 2016), finite-volume-based immersed boundary method and finite-volume-based penalty method (Brändle de Motta *et al.* 2019). It has also been used to conduct wall-bounded turbulent particle-laden studies in both plane channels and circular pipes (e.g. Peng, Ayala & Wang 2019*b*; Peng & Wang 2019; Yang *et al.* 2021). Readers are directed to those cited references for more details of the numerical method.

The previous versions of our LBM–IBB codes did not consider the tangential components of the interaction forces in particle–particle and particle–wall collisions. As we pay more attention to the behaviour of particle motion in the present study, we further refine our codes by adding this ingredient. This refinement was also motivated by a recent study suggesting that excluding the tangential forces could result in non-trivial impacts on the flow and particle statistics in particle-laden turbulent channel flow simulations (Xia *et al.* 2020). The soft-sphere collision model recently reported by Rettinger & Rüde (2022) was adopted since it used LBM–IBB as the simulation method, the same as the present study. This model is a simplified version of the soft-sphere collision model of Costa *et al.* (2015) by omitting the particle rotation matrix when calculating the tangential overlap. We have validated this model based on our in-house codes following the test cases and parameters provided by Costa *et al.* (2015). The results are shown in figures 2 and 3.

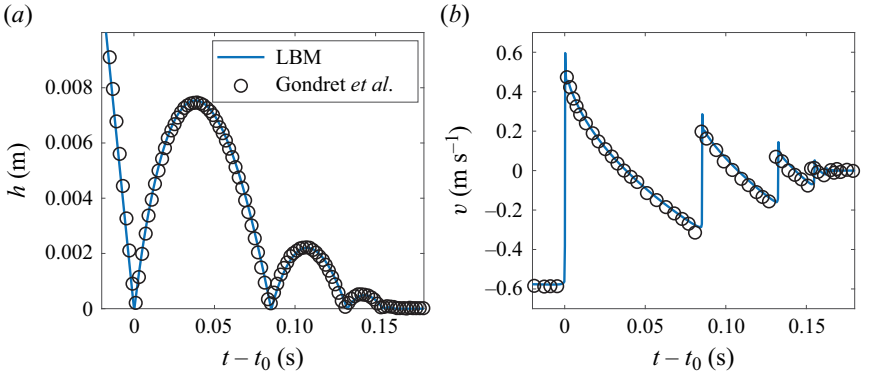

Figure 2. Comparison of (*a*) the particle trajectory and (*b*) the velocity with the experimental results of Gondret, Lance & Petit (2002) in the case of a steel particle colliding and bouncing from a flat wall in viscous fluids. The simulation set-up is similar to that adopted in Costa *et al.* (2015). The overshoots of bounce-back velocity are probably due to the weak compressibility of the LBM that leads to errors in pressure restoration in the narrow gap formed by the particle–wall collision, which does not affect the overall correctness of the trajectory and velocity prediction.

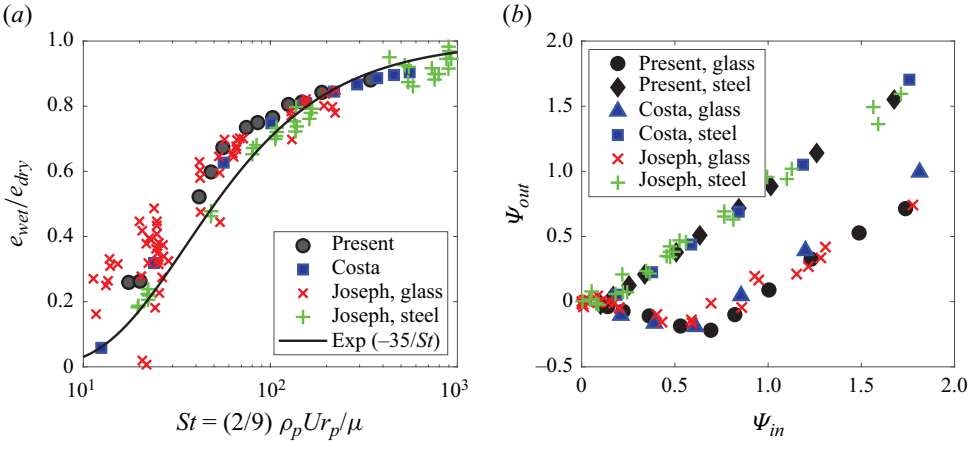

Figure 3. Comparison of particle restitution coefficients in (*a*) normal and (*b*) oblique particle–wall collisions with the experimental results of Joseph (2003) and numerical results of Costa *et al.* (2015). Parameters e_{wet} and e_{dry} are the wet and dry coefficients of restitution, respectively, and Ψ_{in} and Ψ_{out} are the effective angles of incident and rebound.

The values of the friction coefficients and dry-collision restitution coefficients provided in table IV of Costa *et al.* (2015) are used in the later simulations of turbulent channel flows laden with glass and steel particles. For neutrally buoyant particles, those parameters are missing, so we set them to be the same as those for the glass particles.

Detailed elaborations of the numerical approach are not provided. Here, we only summarize some key numerical parameters used in our simulations. The computational domain for all simulated cases spans roughly $L_x \times L_y \times L_z = 12h \times 2h \times 4h$ using a uniform cubic mesh of $1800 \times 299 \times 600$. This mesh results in a grid resolution of $\Delta^+ = 1.204$. Unless otherwise specified, the parameters and results presented in this paper with superscripts '+' are normalized by the friction velocity u_τ and the wall unit $y_\tau = \nu/u_\tau$ in the unladen single-phase case. As reported in our previous studies, LBM

simulations under this grid resolution ensured good comparisons of turbulent statistics with the benchmark results obtained with high-order computational methods, such as spectral methods (Peng 2018).

The PR-DNS are quantitatively reliable only when the grid resolutions representing particles are sufficient, i.e. $d_p/\Delta x$ is large enough. With the selected mesh, the grid resolution representing particles is $d_p/\Delta x = 24$ in most cases. This resolution is sufficient to resolve most of the fluid–particle interactions according to our previous tests (Peng *et al.* 2019*b*; Peng & Wang 2019) and is also comparable to those used in some other relevant studies (e.g. Kidanemariam *et al.* 2013; Picano, Breugem & Brandt 2015; Eshghinejadfard *et al.* 2018; Zhu *et al.* 2020). The only exception is Case B1-R-S which uses a much lower grid resolution $d_p/\Delta x = 8$. Caution must be taken for this particular case when drawing quantitative conclusions. For this reason, we only try one simulation with this low grid resolution to show qualitatively how the particle size affects PA.

3. Results and discussion

3.1. *Phenomena of particle PA*

The results presented in this section are gathered after the fluid–particle systems reached the statistically stationary state. The fluid statistics are time-averaged over 30 large-eddy turnover times ($t_{ave} > 30h/u_\tau$) for roughly 1000 time frames. The particle statistics are also gathered during approximately the same period. However, since the particle information would only be recorded when a particle meets the criteria of 'the particle positioned within the streaks', the sample sizes of particle statistics vary by case. Before showing any results, we need to define those criteria. First, the near-wall plane of $y^+ = 9.0$ is chosen as the 'streak plane', which is used throughout the paper. This plane is close to the upper range of wall-normal locations below which the streak distributions of the streamwise velocity are most profound (Moin & Kim 1982; Moin & Spalart 1987). We emphasize that this streak plane at $y^+ = 9.0$ is not chosen for rigorous quantification purposes but provides convenience for discussions. Since particles investigated in the present work have finite sizes, i.e. $d_p^+ = 28.9$ ($r_p^+ = 14.45$) in most cases, any particles centred in $14.45 < y_c^+ < 23.45$ are crossed by the streak plane. To ensure only particles staying sufficiently close to the wall are counted in the statistical computation of particle positioning, we include only those particles whose surface-to-wall distances are less than $0.15d_p$ from the nearest channel wall for cases with large-size particles ($d_p^+ = 28.9$), meaning that the distance between the particle centre and the chosen plane $y^+ = 9$ is less than $0.677r_p$ for an adequate particle cross-section. In Case B1-R-S with small-size particles ($d_p^+ = 9.6$), the streak plane crosses particles centred between $4.8 < y_c^+ < 13.8$. We count particles with centres below the streak plane $y^+ = 9.0$ as the near-wall particles contributing to the statistical computation. These criteria do not hold rigorous physical meanings but bring convenience to filter out particles with small cross-sections in the streak plane. In the cases with non-settling particles, particles appearing near both channel walls are used in the statistical computation, whereas in the cases with settling particles, only the particles near the bottom wall are considered despite some particles occasionally appearing near the top wall. Unless otherwise specified, the above criteria to pick out near-wall particles in the statistical computation are used throughout the paper.

As a start, snapshots of particles positioning in the streak plane are presented in figures 4 and 5. The filled circles represent the cross-sections of near-wall particles whose information is recorded for later statistical computation according to the criteria elaborated above, whereas the open circles represent the cross-sections of other particles

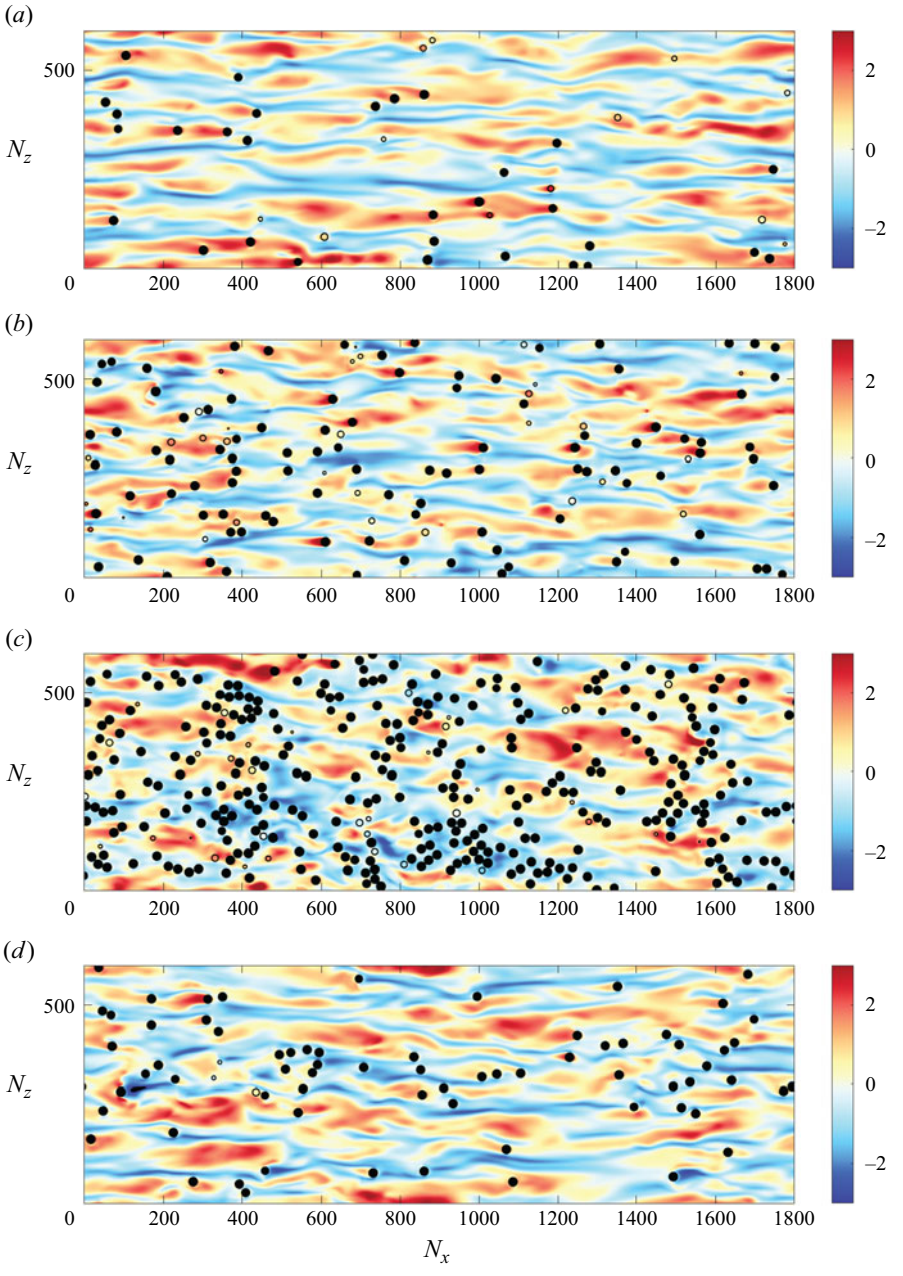

Figure 4. Snapshots of particle distributions in the streak plane: (*a*) Case C0, (*b*) Case C1, (*c*) Case C2, (*d*) Case C2-R. The contour levels are the normalized streamwise velocity $(u - \langle u \rangle)/u_{rms}$ in each case.

crossed by the streak plane. For conciseness, figure 4 only shows the snapshots of particle distributions in the streak plane in the four cases with steel-like particles, i.e. Case C0 to Case C2-R in table 1. Except for Case C2 with strong settling effect $\Theta = 0.2$ and a relatively large particle volume fraction of $\phi_p = 1.5\,\%$, where particles induce significant flow modulation, turbulent structures of alternate LSS and HSS are preserved. Under no

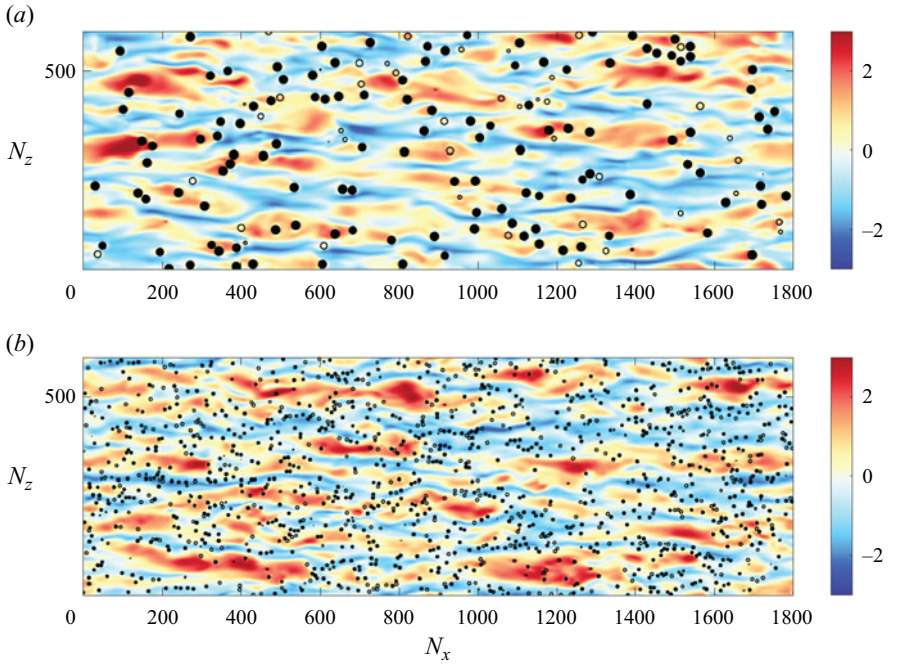

Figure 5. Comparison of particle distributions in the streak plane with different particle sizes. (*a*) Case B1 with large particles $d_p^+ = 28.9$. (*b*) Case B1-R-S with small particles $d_p^+ = 9.6$.

settling and weak settling effects, particles appear more frequently in HSS (figure 4*a*,*b*). When the settling effect increases, particles tend to gather more in LSS.

Figure 5 compares the distributions of large and small particles in the streak plane. The two contrasted cases have an identical density ratio of $\rho_p/\rho_f = 2.5$ and are subject to the same sedimentation effect $\Theta = 0.907$. Unlike most large particles preferentially accumulating in HSS, small particles are often observed in LSS. The latter phenomenon is consistent with most of the studies reported in the literature with relatively small particle sizes, as reviewed in § 1. The trend that PA in LSS disappears (or even reverts into PA in HSS) as the particle size increases also agrees qualitatively with the observation by Niño & Garcia (1996).

Compared with the above visualizations showing intuitive pictures of how particles distribute in near-wall streaks, turbulent statistics can provide more reliable quantifications of PA due to the intermittency of turbulent flows. The studies of Pedinotti *et al.* (1992) and Kidanemariam *et al.* (2013) are among the very few reported statistics of PA. The former research used the ratio between the averaged streamwise velocity at the particle locations and the mean flow velocity in the streak plane as the quantifier of PA. The smaller this ratio is, the more particles accumulate in LSS. This approach is unsuitable for cases in the present study since the fluid velocity at the particle location is not well defined with finite-size particles. In the study of Kidanemariam *et al.* (2013), PA is quantified by the streamwise velocity distribution in the streak plane as a function of spanwise separation from the particle centre, i.e.

$$U_f(z') = \langle u^i(x', z', t)\rangle^{p,t,x'}, \quad u^i(x', z', t) = u(x, y^+ = 9.0, z, t), \tag{3.1a,b}$$

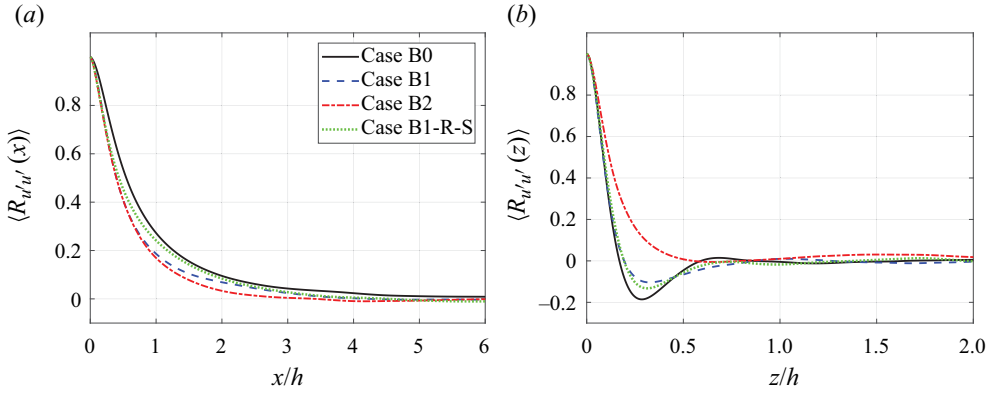

Figure 6. Auto-correlation function of the streamwise fluctuation velocity in the streak plane. (*a*) Streamwise correlation. (*b*) Spanwise correlation.

where $x' = x^i - x$, $z' = z^i - z$ are the streamwise and spanwise distances from the centre of the ith near-wall particle to a fluid node in the streak plane $(x, y^+ = 9.0, z)$. The superscript p, t, x' means ensemble averaging over the particle samples, time and streamwise separation.

It is evident from the visualizations in figures 4 and 5 that both HSS and LSS have finite streamwise lengths. Therefore, when computing $U_f(z')$, the spatial averaging in the streamwise direction should be over an appropriate streak length L rather than the whole channel length $12h$. The streak lengths and widths in different cases can be estimated from the auto-correlation functions of the streamwise fluctuation velocity in the streamwise and spanwise directions, respectively, as shown in figure 6. These results confirm that the flow structures of alternate HSS and LSS still dominate the near-wall turbulence even with the presence of the particles, except in Case B2, where particles significantly modify the near-wall turbulence under a strong sedimentation effect. However, we may still estimate the length and width of streaks as $L = 4h$ and $W = 0.3h$, respectively. Using $L = 4h$ in the computation of U_f, i.e. only counting $|x'| \leq 2h$ in the streamwise averaging in (3.1*a*,*b*), the spanwise profiles of U_f for different cases are shown in figure 7. To better compare these results, we subtract the mean value of $\langle U_f(z')\rangle^{z'}$ and normalize them by the root-mean-square (r.m.s.) velocity in the streak plane in each case.

As shown in figure 7(*a*), in the cases with non-settling and weakly settling particles, the profiles of U_f are above the average when Δz^+ is small, which confirms that the fluid around particles has higher velocity than its average, i.e. particles accumulate in HSS. When using the differences between the highest and lowest points of U_f in the profiles to measure the degree of PA, the neutrally buoyant particles exhibit the most profound PA. When the particle inertia increases, i.e. from neutrally buoyant particles to glass and steel particles, the degree of PA in HSS decreases. The sedimentation effect also weakens PA in HSS. Although a weak sedimentation effect is insufficient to revert the qualitative picture, the degrees of PA (quantified by the maximum difference in U_f profile) in the corresponding cases are further reduced compared with the corresponding cases with non-settling particles.

On further enhancing the sedimentation effect, the values of U_f with small Δz^+ drop below the average, meaning that the PA location moves from HSS to LSS. These statistics confirm the intuitive pictures of PA observed from the visualizations in figure 4. However, the lowest value of U_f does not occur at $\Delta z^+ = 0$, but is shifted to $\Delta z^+ \approx 15$, roughly

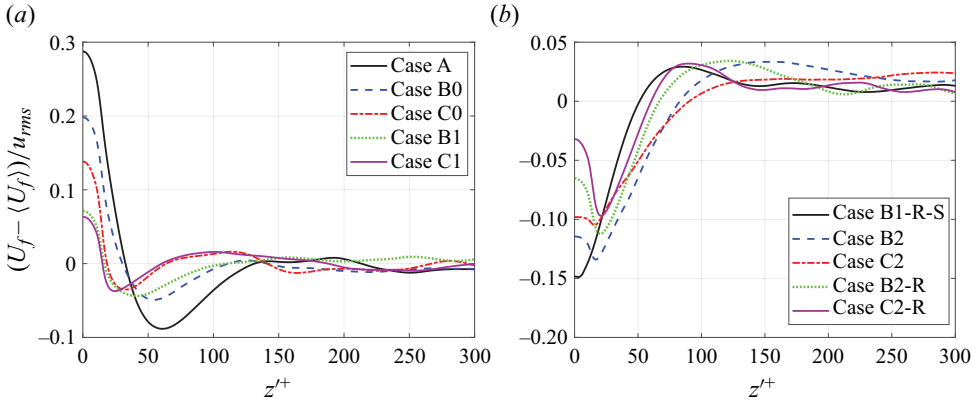

Figure 7. Spanwise distribution of the mean flow velocity in the streak plane. (*a*) Cases where particles preferentially accumulate in HSS. (*b*) Cases where particles preferentially accumulate in LSS.

corresponding to one particle radius ($r_p^+ = 14.5$). The reason for not having the lowest value of U_f at $\Delta z^+ = 0$ is that when gathering the statistics of U_f, particles just entering the near-wall locations with high initial velocity are also counted. Since particles have a finite size and large inertia ($\tau_p^+ = (\rho_p/\rho_f)(d_p^+)^2/18 = 116$ and 362 for the glass and steel particles in the present study), they can significantly accelerate the fluid velocity around them with their high initial momentum gained from outside the near-wall region. This fact is supported by the animations of particle motion in the streak plane, which are provided in the supplementary material and movies available at https://doi.org/10.1017/jfm.2024.41 for a few selected cases. The two cases with the low particle volume fraction, Case B2-R and Case C2-R, have larger fluid velocities outside the near-wall region than Case B2 and C2, i.e. $\langle u \rangle^+ = 9.64$ and 9.62 compared with 7.33 and 5.46 at $y^+ = 15$. As a result, their drops of U_f from $\Delta z^+ = 0$ to the minimum values are also higher. Since the newly entered small particles in Case B1-R-S have lower capabilities to accelerate their ambient fluids, the location of the minimum U_f moves closer to the y axis, and the drop of U_f further shrinks in the corresponding profile.

Despite the weaker sedimentation effect, the small particles in Case B1-R-S show the most profound PA in LSS. This observation indicates that the particle size has the most significant impact on PA. Similar to PA in HSS, PA in LSS decreases when the density ratio increases. The gaps between the highest and lowest U_f in Case C2 and Case C2-R are narrower than in Case B2 and Case B2-R. The particle volume fraction also plays a role in the quantitative levels of PA in LSS. Cases B2 and C2 with higher particle volume fraction show more profound PA than their corresponding cases with lower particle volume fractions. This difference could also be a result of flow modulation. Like the flow acceleration due to high-speed particles from outside the near-wall region, strongly settling particles that linger in the near-wall regions for sufficiently long times could also gain low velocities and decelerate the fluid around them. With higher volume fractions, particles could form clusters and amplify this deceleration effect, eventually leading to more particles located in LSS.

3.2. *Mechanisms for particle preferential accumulation*

In terms of mechanism, PA in LSS has been well understood. As demonstrated in figure 1, the spanwise sweeping was widely regarded as the main mechanism (Niño & Garcia 1996;

Kidanemariam *et al.* 2013). Marchioli & Soldati (2002) identified another mechanism of PA in LSS. Some counter-rotating vortices above LSS could prevent particles from being entrained by the ejection events and trap particles in LSS, which further reinforces PA in LSS.

On the contrary, mechanisms leading to PA in HSS are less understood. Through visualizations, Do-Quang *et al.* (2014) found that the interactions between finite-size fibres and the channel wall made fibres resist the spanwise sweeping and remain in HSS. Eshghinejadfard *et al.* (2018) later adopted the same reason to explain the PA of large spheroid oblates and spherical particles in HSS. However, this mechanism cannot explain the present results since the settling particles subjected to more frequent particle–wall interactions are less frequently observed in HSS. Xia *et al.* (2021) provided another explanation for the PA of finite-size particles in HSS. This explanation came from the observation that particles accumulated in HSS in the upward turbulent channel flows but in LSS in downward turbulent channel flows. Unlike the downward turbulent channel flows, particles tend to move toward the channel centre in the upward channel flows under the effect of Saffman lift (Saffman 1965). Xia *et al.* (2021) deduced that particles moving away from the wall could experience the anti-spanwise sweeping from the quasi-streamwise vortices that drove particles to HSS. However, the quasi-streamwise vortices mainly centre around $y^+ = 20$ with a radius of $r^+ \approx 15$ (Kim *et al.* 1987), which means the anti-spanwise sweeping is most likely to happen in the range of $20 \leq y^+ \leq 35$, which is above the streak plane typically located at $y^+ \leq 10$.

As discussed earlier, unlike small particles that passively position in the near-wall streaks, large particles with sufficiently high streamwise velocities can create HSS by themselves. This mechanism partially leads to the observation of PA in HSS, and it also explains why PA in HSS was only reported in the literature when the particle sizes were sufficiently large (Do-Quang *et al.* 2014; Eshghinejadfard *et al.* 2018; Zhu *et al.* 2020). However, this mechanism of flow acceleration only applies to those particles newly entering the near-wall region, and it cannot justify the impact of particle density and sedimentation effect on PA. The explanations for particles accumulating preferentially in HSS still need further exploration.

Since the particle distribution is determined by the hydrodynamic force, to understand better the reasons causing PA in the spanwise direction, we first analyse the statistics of spanwise hydrodynamic forces acting on the near-wall particles. The spanwise momentum equation of the fluid phase reads

$$\rho\frac{\partial w}{\partial t}+\rho\frac{\partial (uw)}{\partial x}+\rho\frac{\partial (vw)}{\partial y}+\rho\frac{\partial (ww)}{\partial z}=\frac{\partial \sigma_{xz}}{\partial x}+\frac{\partial \sigma_{yz}}{\partial y}+\frac{\partial \sigma_{zz}}{\partial z}-F_z, \tag{3.2}$$

where u, v and w are the streamwise, wall-normal and spanwise velocity components, respectively, and σ_{xz}, σ_{yz} and σ_{zz} are the three total stress components associated with the spanwise momentum. Force F_z is the hydrodynamic force acting on the particles by the fluid phase. To find out how particles distribute in the near-wall streaks, we apply a special time averaging over a particular time interval t_s, where t_s is larger than the particle response time τ_p but smaller than the lifespan of a pair of alternate near-wall streaks. Under this special time averaging, $\langle F_z\rangle^{t_s}$ reads

$$\langle F_z\rangle^{t_s}=-\rho\left[\frac{\partial \langle uw\rangle^{t_s}}{\partial x}+\frac{\partial \langle vw\rangle^{t_s}}{\partial y}+\frac{\partial \langle ww\rangle^{t_s}}{\partial z}\right]+\left[\frac{\partial \langle \sigma_{xz}\rangle^{t_s}}{\partial x}+\frac{\partial \langle \sigma_{yz}\rangle^{t_s}}{\partial y}+\frac{\partial \langle \sigma_{zz}\rangle^{t_s}}{\partial z}\right]. \tag{3.3}$$

Case	A	B0	C0	B1	C1	B2	C2	B2-R	C2-R	B1-R-S
$Q_{(k_z,u'_x)}$	0.0943	0.0878	0.0811	0.0706	0.0620	0.0868	0.1119	0.0751	0.0706	0.0866

Table 2. Correlation between the spanwise TKE k_z and the streamwise r.m.s. velocity u_{rms} in the streak plane $y^+ = 9$.

In turbulent channel flows, the mean velocity and pressure gradient in the wall-normal and spanwise directions vanish after averaging over a sufficiently long period, i.e. $\langle v\rangle = \langle w\rangle = 0$ and $\partial\langle p\rangle/\partial z = 0$, which also leads to $\langle\sigma_{yz}\rangle = \mu(\partial\langle v\rangle/\partial z + \partial\langle w\rangle/\partial y) = 0$. Since t_s is below the lifespan of a pair of near-wall streaks, those conditions are only approximately valid. However, the experimental measurements of Smith & Metzler (1983) showed that the near-wall streaks were highly persistent and could last for about $480\nu/u_\tau^2$ on average, which translates to a few large-eddy turnover times. For this reason, the above approximations should not result in significant errors. Moreover, since the flow in the streamwise direction is homogeneous, the gradients in the streamwise direction x can also be removed. After applying the Reynolds decomposition and ignoring the trivial Reynolds stress component $\langle v'w'\rangle^{t_s}$, (3.3) is simplified as

$$\langle F_z\rangle^{t_s} \approx -\rho\frac{\partial\langle w'w'\rangle^{t_s}}{\partial z}. \tag{3.4}$$

The above analysis indicates the particle motion in the spanwise direction is under the influence of 'turbophoresis', a widely recognized turbulence effect on particle motion that drives particles from regions of high to low turbulent kinetic energy (TKE) (Reeks 1983). In wall-bounded turbulent flows, turbophoresis is often invoked to explain the tendency of particles to migrate towards the wall (Sardina *et al.* 2012). Here, we extend its definition since the tendency of particles to accumulate in the near-wall streaks is also associated with the non-uniform distribution of TKE among those streaks. The influence of turbophoresis on PA can be understood as follows. Considering particles randomly walking in the streak plane, particles surrounded by more energetic fluids are more likely to move away from their initial locations, whereas particles originally sited around less energetic fluids have less momentum to leave. Since HSS are regions created by sweeping events that carry more energetic fluids from the outer region, the spanwise TKE in HSS is higher than that in LSS containing low-TKE fluids due to the ejection events from the viscous sublayer.

In table 2, we show the averaged correlation coefficient between the streamwise r.m.s. velocity u_{rms} and the spanwise TKE $k_z = 0.5\langle w'w'\rangle$ in the streak plane $y^+ = 9$, i.e.

$$Q_{(k_z,u'_x)} = \frac{\langle k_z u_{rms}\rangle^{x,z,t}}{\langle k_z\rangle^{x,z,t}\langle u_{rms}\rangle^{x,z,t}}, \tag{3.5}$$

in each case. The positive correlations confirm that the fluid has greater spanwise TKE in HSS than in LSS. With this statistical distribution of spanwise TKE, particles should tend to move toward LSS under turbophoresis.

With the above understanding, we can more confidently deduce why large particles accumulate in HSS under no or weak sedimentation effects. When particles have large sizes, their hydrodynamic forces are also contributed by the fluid motion outside the streak plane, which may have the opposite spanwise TKE gradient contrasting to the streak plane. As shown in figure 8, the spanwise TKE maximizes around $y^+ = 30$, which implies that

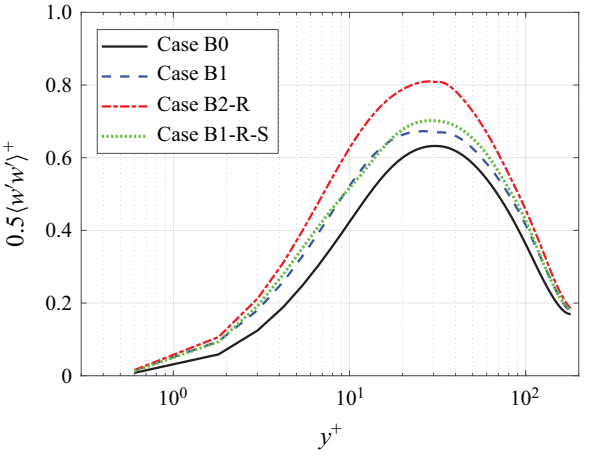

Figure 8. Wall-normal distribution of spanwise TKE.

Case	A	B0	C0	B1	C1	B2	C2	B2-R	C2-R	B1-R-S
$\langle d\rangle/d_p$	0.0873	0.0839	0.0774	0.0766	0.0704	0.0544	0.0423	0.0626	0.0611	0.2449
$\langle d^+\rangle$	2.524	2.425	2.236	2.214	2.034	1.572	1.222	1.809	1.766	2.359

Table 3. The averaged distance of counted near-wall particles from channel walls.

the greater spanwise TKE is more likely to be observed in the high-speed regions below this plane, whereas the opposite could occur when $y^+ > 30$. As a result, large particles covering a wide range of y locations respond with more difficulty to turbophoresis. We can also view this mechanism from the different responses to the spanwise sweeping by large and small particles. Unlike small particles that can be fully contained between $5 \leq y^+ \leq 20$, where the streamwise vortices consistently sweep from HSS to LSS (Kim *et al.* 1987), large particles with a size comparable to the streamwise vortices ($r^+ \approx 15$) are subject to both spanwise and anti-spanwise sweeping, which reduces their spanwise mobility in the near-wall region.

Following the same logic, we can understand why particles under strong sedimentation effects tend to accumulate more in LSS. Under strong sedimentation effects, particles can gather closer to the channel wall, where the spanwise sweeping from HSS to LSS dominates, which makes them more likely to move toward LSS. In table 3, we compute the average gap distances between the particle surfaces and the nearest channel wall in different cases. As expected, particles appear more closely to the channel wall under more intensive gravitational effects. The particle inertia also plays a specific role in the equilibrium location of particles. Under the same Shields number, particles with higher density ratio can move further towards the wall. This is because the equilibrium location of particles results from the balance between the lift forces and particle–wall interactions (Peng *et al.* 2019*b*). The latter factor is closely related to the particle velocity and particle–wall gap distance, not the particle density (Brenner 1961). For this reason, particles with larger densities experience stronger resistance when pushed away from the wall by the particle–wall interactions. Thus, they can gather more closely to the channel walls.

To quantitatively support the above deductions, i.e. that spanwise sweeping does not dominate the distribution of large particles and the sedimentation effect can reinforce PA in LSS, we propose the following methods to quantify the impact of spanwise sweeping in different cases. As expected, spanwise sweeping happens when there is a spanwise relative motion, or 'slip velocity', between a particle and its ambient fluid, i.e. $w_f - w_p \neq 0$. Therefore, we may use the slip velocity in the spanwise direction to assess spanwise sweeping. When the statistical correlation between $w_f - w_p$ and the spanwise hydrodynamic force is more considerable, the spanwise sweeping makes a more significant contribution.

However, accurately defining the slip velocity is always tricky for finite-size particles since the undisturbed fluid velocity is absent at the particle location. In this analysis, we follow the method proposed by Kidanemariam *et al.* (2013) to assess the slip velocity, where the fluid velocity around a particle is defined as the average velocity on a concentric shell outside the particle surface. Alternative but similar methods can also be found in, for example, Lucci, Ferrante & Elghobashi (2010), Cisse, Homann & Bec (2013) and Brändle de Motta *et al.* (2019), which also calculate the slip velocity based on the fluid velocity on concentric shells but different in details. However, these alternative methods are less suitable for wall-bounded turbulence, as they did not exclude the part on the shell that is beyond the wall-normal range covered by the particle, i.e. $y < y_c - 0.5d_p$ and $y > y_c + 0.5d_p$, where y_c is the wall-normal location relative to the particle surface, to consider the flow inhomogeneity in the wall-normal direction.

Choosing the appropriate shell radius r_s is crucial in defining the slip velocity. On the one hand, r_s should be large enough to avoid strong disturbance from the particle. If $r_s = r_p$, the slip velocity defined with the method of Kidanemariam *et al.* (2013) is 0. On the other hand, r_s should not be overestimated in cases with multiple particles, so the influence from other nearby particles can be neglected. The study of Kidanemariam *et al.* (2013) chose a shell radius $r_s = 3r_p$ based on the results of flow velocity recovery in the case of uniform flow passing through a fixed sphere. With this shell radius, the average velocity on the shell recovered about 90 % of the incoming flow velocity at various particle Reynolds numbers (Kidanemariam *et al.* 2013). Another study by Naso & Prosperetti (2010) measured the 'region of influence' of a fixed particle in homogeneous isotropic turbulence. They found that beyond $r_s = 4r_p$, the variation, skewness and flatness of the fluid velocity were no longer modified significantly by the particle at a particle Reynolds number of around 20. It should be noted that both previous studies chose their appropriate shell radii based on the fluid–particle interactions of isolated particles. In simulations with multiple particles, r_s should be reduced from the value for isolated particles, say $r_s = 3r_p$, to minimize the impact from other particles. However, finding the optimal r_s becomes more challenging. Our strategy is to choose different r_s to evaluate the spanwise slip velocity $w_f - w_p$. Besides $r_s = 3r_p$, two smaller shell radii, i.e. $2.0r_p$ and $2.5r_p$, are chosen. The thickness of these shells is always kept as one grid spacing or $\delta^+ = 1.2$.

After defining the slip velocity, we can assess the contribution of spanwise sweeping on the particle motion. Contours of the joint probably distribution functions (PDFs) of the spanwise slip velocity and the actual spanwise hydrodynamic force are presented in figures 9–11 for three different shell radii, $r_s = 2.0r_p$, $2.5r_p$ and $3.0r_p$, respectively. Only the results from three representative cases with glass particles, i.e. Cases B0, B2 and B1-R-S, are presented for conciseness. The joint PDFs show similar contours with different choices of r_s, indicating that the correlations between the spanwise hydrodynamic force and the spanwise slip velocity are not, at least qualitatively, affected by the specific

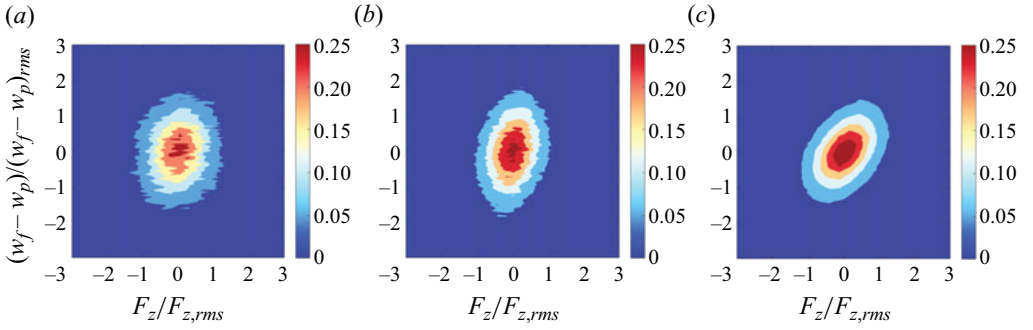

Figure 9. Joint PDF of the slip velocity and the hydrodynamic force in the spanwise direction in (*a*) Case B0, (*b*) Case B2 and (*c*) Case B1-R-S. The slip velocity is quantified based on the shell-averaged velocity on the concentric shell with a radius of $r_s = 2.0r_p$. The thickness of the shell δ is equal to one grid spacing or $\delta^+ = 1.2$.

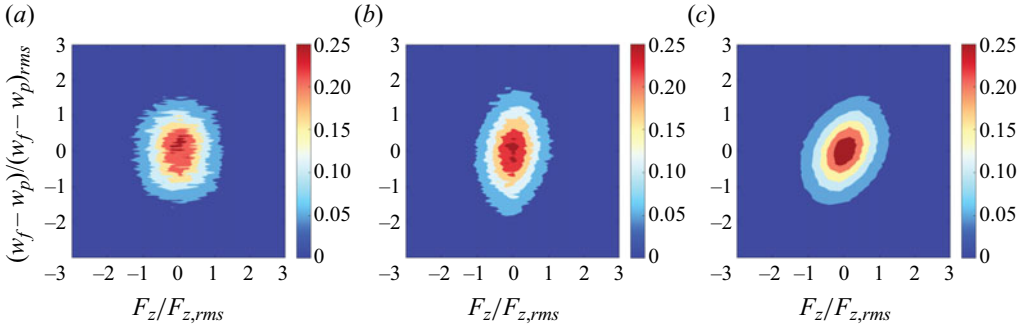

Figure 10. Same as figure 9 but with $r_s = 2.5r_p$.

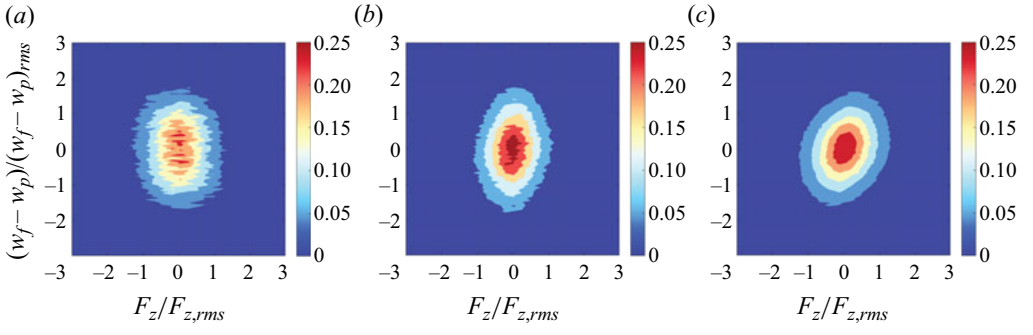

Figure 11. Same as figure 9 but with $r_s = 3.0r_p$.

choice of r_s. Since particles do not appear frequently in the near-wall regions without gravity and the number of particles is relatively small for large particles, the joint PDFs in Case B0 are somehow noisy due to insufficient sampling (Case B0 uses 46 653 samples, whereas Cases B2 and B1-R-S use 81 388 and 343 932 samples, respectively, leading to much smoother contours).

In Case B0, the joint PDFs (left-hand panel of each of figures 9–11) are almost un-tilted. This confirms our previous deduction that large particles do not statistically respond to spanwise sweeping when the sedimentation effect is absent or weak.

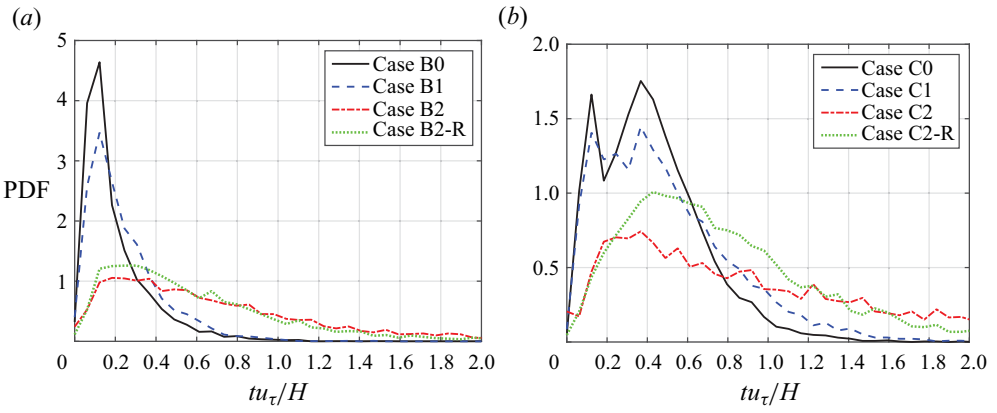

Figure 12. The PDFs of the particle residence time in the near-wall region. (*a*) Glass particle cases. (*b*) Steel particle cases.

The uncorrelated results also imply that PA in HSS is not a result of anti-spanwise sweeping, as deduced previously by Xia *et al.* (2021). The joint PDFs tilt slightly to the first and third quadrants (middle panel) in Case B2 with the settling of large particles. These results validate that when particles gather very close to the wall under gravity, the spanwise sweeping mechanism statistically contributes to the spanwise hydrodynamic force, which is responsible for PA in LSS. In Case B1-R-S with small particles, although the sedimentation effect is weaker than in Case B2, the joint PDFs of spanwise slip velocity and particle force still strongly tilt to the first and third quadrants (right-hand panel), which shows that the spanwise sweeping is indeed the dominating mechanism for PA of small particles.

Aside from resulting in lower equilibrium locations that amplify the contribution of spanwise sweeping, the settling effect also provides resistance to the particle–wall interactions and ejection events that lift particles away from the near-wall regions, so particles are more frequently observed in LSS. This mechanism is implied in the animations provided in the supplementary material. Without gravity, i.e. in Case B0, particle–wall interactions lift most particles away from the near-wall regions before they migrate to the edges of LSS, due to either directional spanwise sweeping or random walking (since both sides of an HSS are LSS). The particles that reach LSS would also leave the near-wall region quickly since they cannot resist the intense ejection events forming LSS. On the contrary, with the help of gravitational sedimentation, particles in Case B2 can migrate further to LSS and stay there longer.

To show this point more clearly, we compute the PDFs of the particle residence time in the near-wall region. When a particle enters and leaves the near-wall region, its duration in the near-wall region is recorded, and the travelled spanwise distance during this duration is computed. Since case B1-R-S with small-size particles uses a different criterion to identify the near-wall particles, the corresponding results in this case are omitted.

As shown clearly in figure 12, compared with particles under no or weak sedimentation effect, i.e. Cases B0, B1, C0 and C1, strongly settling particles have a significantly higher possibility of staying in the near-wall regions for more extended periods. The particle inertia also plays a role in determining the residence time. In table 4, we show the averaged residence times in each simulated case. Steel particles with greater inertia have significantly longer residence time than glass particles, with and without the settling effect. On the other hand, the strong sedimentation effect results in similar relative extensions

Case	A	B0	C0	B1	C1	B2	C2	B2-R	C2-R
N	4460	7148	4461	3795	3797	3500	4462	3738	3112
tu_τ/H	0.24	0.23	0.45	0.27	0.52	0.74	1.41	0.63	0.82
Δz^+	19.15	21.07	35.94	23.52	39.55	47.35	64.39	45.46	58.35

Table 4. Averaged residence time of particles in the near-wall region and the moved spanwise distance during the residence time. The sample sizes N of each case to compute those statistics are given in the first row.

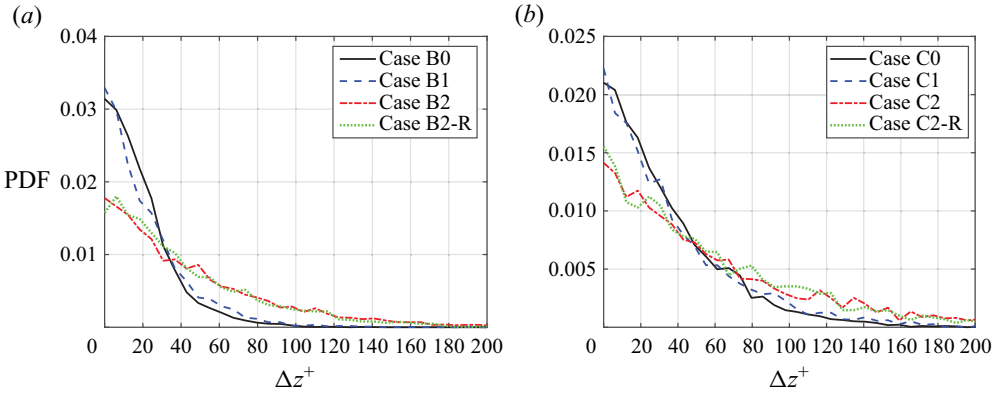

Figure 13. The PDFs of the travelled spanwise distance during the particle residence time. (*a*) Glass particle cases. (*b*) Steel particle cases.

of the residence time in the near-wall region for glass and steel particles. The averaged residence times are increased by 221 % and 213 % for the glass and steel particles from no sedimentation to strong sedimentation cases, respectively, which are close. This similarity could be because the two cases with strong sedimentation effect have the same Shields number, although their particle inertias are different. We thus infer that the Shields number is a suitable indicator for the influence of the sedimentation effect on the PA phenomenon.

Due to the shorter residence times in the near-wall region, the probabilities for non-settling and weakly settling particles to travel long distances in the spanwise direction are also lower, as demonstrated in figure 13. As one could realize earlier from figure 6(*b*), the average distance between HSS and their nearby LSS is roughly $W = 0.3h$ or $W^+ = 54$. Since a significant part of non-settling and weakly settling particles would exit the near-wall region after only travelling short distances, they would spend their whole lifetime in HSS, eventually leading to the observation of PA in HSS. On the contrary, when a strong sedimentation effect is present, the averaged spanwise travelled distances are nearly doubled for both glass and steel particles, as shown in the last row of table 4. For this reason, particles initially entering the near-wall regions through HSS are more likely to be found in LSS, resulting in the opposite PA observation.

It is well documented in the literature that sedimenting particles in wall-bounded turbulence can experience different modes of motion, such as rolling, saltation and resuspension (Ji *et al.* 2014; Yousefi *et al.* 2020). The data shown in table 4 can be potentially used to model how particle inertia and the sedimentation effect modify the locations and levels of PA. However, building such a predictive model is beyond the scope of the present work since its primary purpose is to reveal the PA mechanisms of large-size particles in HSS. We may conduct more systematic studies in this direction in the future.

	Flow	Type of investigation	Sediment particles?[a]	Particle size d_p^+	Density ratio ρ_p/ρ_f	Accumulation location
Rashidi *et al.* (1990)	Horizontal full channel	Experiments	Yes	0.9–11.8	1.03–2.5	Low-speed streaks
Pedinotti *et al.* (1992)	Horizontal open channel	Point-particle DNS	Yes	1.29–11.8	1.03	Low-speed streaks
Niño & Garcia (1996)	Horizontal open channel	Experiments	Yes	4.3–7.7	∼2.65	Low-speed streaks
Pan & Banerjee (1996)	Horizontal open channel	Point-particle DNS	Yes	1–4	1.05	Low-speed streaks
Suzuki *et al.* (2000)	Downward vertical channel	Experiments	No	4.1	∼3.85	Low-speed streaks
Marchioli & Soldati (2002)	Upward vertical channel	Point-particle DNS	No	0.3–1.65	769.3	Low-speed streaks
Shao *et al.* (2012)	Horizontal full channel	Fully resolved DNS	Yes	21–42	1.5	Low-speed streaks
Kidanemariam *et al.* (2013)	Horizontal open channel	Fully resolved DNS	Yes	7.21	1.7	Low-speed streaks
Eshghinejadfard *et al.* (2018)	Horizontal full channel	Fully resolved DNS	No	27.69	1	High-speed streaks
Fong *et al.* (2019)	Downward vertical channel	Experiments	No	0.78–1.1	2083	Low-speed streaks
Zhu *et al.* (2020)	Upward vertical channel	Fully resolved DNS	No	18	2	High-speed streaks
Xia *et al.* (2021)	Downward vertical channel	Fully resolved DNS	No	∼18.8	2	Low-speed streaks
Yang *et al.* (2021)	Downward vertical channel	Fully resolved DNS	No	∼30	1.15	Low-speed streaks
Berk & Coletti (2023)	Plane boundary layer	Experiments	Yes	0.4–3.6	∼1969	Low-speed streaks

Table 5. Preferential accumulation phenomena reported in the literature.

[a]Here the sediment effect means particles are subject to the gravitational effect in the wall-normal direction.

Finally, to complete the discussion, we summarize the observations of PA reported in some representative previous studies in table 5, and examine if the mechanisms discussed above can support these observations. Since the particle size, density ratio and sedimentation effect are the three key factors affecting PA, we include this information in table 5. When the sizes of the particles are relatively small ($d_p^+ \lessapprox 10$), spanwise sweeping dominates the spanwise migration of particles in the near-wall region, so PA in LSS can be observed with and without the sedimentation effect. This is consistent with the observations reported in Rashidi *et al.* (1990), Pedinotti *et al.* (1992), Niño & Garcia (1996), Pan & Banerjee (1996), Suzuki *et al.* (2000), Marchioli & Soldati (2002), Kidanemariam *et al.* (2013), Fong *et al.* (2019) and Berk & Coletti (2023). When the

sizes of particles become large, PA in either LSS or HSS can appear, depending on other factors. When the sedimentation effect is strong, one still observes particles gathering in LSS. This is because the strongly settling particles tend to remain close to the wall sufficiently long, eventually allowing the streamwise vortices to convey particles to LSS. The lower equilibrium locations of sediment particles could also reinforce the effect of spanwise sweeping. Moreover, the large piles of low-speed sediment particles could also decelerate the near-wall fluids and create LSS around them, further strengthening the gathering of particles in LSS. These two mechanisms explain PA of settling large particles in the low-speed regions reported by Shao *et al.* (2012) with a large particle volume fraction $\phi_p = 2.36\,\%$ and $7.07\,\%$. Although the sedimentation effect was absent in the two downward vertical channel flow simulations by Xia *et al.* (2021) and Yang *et al.* (2021), the lift forces would play the same role as the gravitational acceleration and move particles towards the wall. For this reason, large particles in downward vertical channel flows still gather in LSS (Xia *et al.* 2021; Yang *et al.* 2021). The lift forces directing particles towards the wall are less intense in horizontal channel flows and can even revert directions in upward channel flows. As a result, particles quickly leaving the near-wall regions before migrating to LSS would lead to the observation that particles preferentially accumulate in HSS, as reported by Eshghinejadfard *et al.* (2018) and Zhu *et al.* (2020) in the corresponding simulations.

4. Summary and conclusions

The present study was motivated by the need for systematic discussions on the PA of finite-size particles in the near-wall region of wall-bounded turbulence. In particular, although previous studies have extensively revealed the mechanisms responsible for PA in LSS, the reason leading to some recent observations of large particles accumulating in HSS needed to be better understood. This study set up PR-DNS to study how the particle-to-fluid density ratio, sedimentation effect, particle volume fraction and particle size affect the PA of finite-size particles in the near-wall region and to explore the mechanisms for different PA behaviours. The main findings through our PR-DNS are summarized below.

First, under the spanwise sweeping of quasi-streamwise vortices, small inertial particles always gather in LSS. In contrast, large particles can accumulate in either LSS or HSS, depending on the strength of the sedimentation effect. Large-size particles still appear more frequently in LSS when the sedimentation effect is strong enough. When there is no sedimentation effect, or the sedimentation effect is weak, the PA location of large particles switches to HSS. We found that the quantitative degree of PA reduces as the particle-to-fluid density ratio increases. Neutrally buoyant particles show the most significant PA in HSS, followed by glass and steel particles under no and weak sedimentation effects. For strongly settling particles gathering in LSS, the PA of glass particles is also more profound than that of steel particles with a larger density ratio.

Unlike small particles that induce limited turbulence modulation, large particles can significantly modify the near-wall turbulence. Large particles newly entering the near-wall region with a high streamwise velocity can accelerate their ambient fluid and create HSS. On the other hand, particles remaining near the channel wall may move slowly, decelerating the fluids and creating LSS. This mechanism of flow modulation partially explains why large particles are found in HSS and why PA in LSS is more profound with increasing particle volume fractions.

The phenomena of PA in LSS can be understood as a result of turbophoresis in the streak plane, i.e. particles tend to statistically migrate out from HSS with higher spanwise TKE to LSS with lower spanwise TKE. Due to their sizes, large particles are also affected by the distribution of spanwise TKE in other wall-parallel planes beside the streak plane. When particles are small, the wall-normal planes contributing to their spanwise motion still have similar distributions of spanwise TKE, so the overall movement of particles is still from HSS to LSS. However, when particles are sufficiently large, their motion would be affected by wall-normal planes with the opposite distribution of spanwise TKE, generating turbophoresis in the opposite direction. As a result, the statistical migration of particles from HSS to LSS is prohibited, and particles tend to stay in HSS.

Finally, the sedimentation effect significantly impacts the location of PA. It drives particles closer to the bottom wall, reinforcing the spanwise sweeping and resisting particle–wall interactions and ejection events that push particles away from the near-wall regions. Under the strong sedimentation effect, particles enter LSS with less resistance and stay there longer, eventually resulting in PA in LSS.

Different PA behaviours reported in the literature can be better understood with the mechanisms mentioned above. For example, large particles accumulate in LSS in downward channel flows because the lift forces play the role of the sedimentation effect that drives particles toward the wall. In upward channel flows, the lift force reverts its direction, so particles quickly leave the near-wall region before entering LSS, and thus PA in HSS is observed. However, open issues concerning PA still require further investigation. For example, when the sedimentation effect is absent, what is the transition particle size from PA in LSS to PA in HSS? Are there other mechanisms that affect particle accumulation in the near-wall streaks? How do we better quantify the degree of PA and build quantitative models to predict PA based on flow and particle parameters? These questions require more data over wider ranges of flow and particle parameters. Better ways to quantitatively analyse the mechanisms affecting particle motion in near-wall turbulence are also necessary to resolve these open issues.

Supplementary material and movies. Supplementary material and movies are available at https://doi.org/10.1017/jfm.2024.41.

Acknowledgements. The authors thank Dr P. Costa from Delft University of Technology for a discussion on implementing the particle–wall collision models.

Funding. This work has been supported by the National Natural Science Foundation of China (C.P., grant number 12102232; L.-P.W., grant numbers U2241269 and T2250710183; S.C., grant numbers U2006221 and 52176040) and the Natural Science Foundation of Shandong Province, China (C.P., grant numbers ZR2021QA010 and 2022HWYQ-023). Financial support from Shandong University through the Qilu Young Scholar Program is also acknowledged. Computing resources are provided by the National Supercomputing Center at Jinan, and the Center for Computational Science and Engineering of Southern University of Science and Technology.

Declaration of interests. The authors report no conflict of interest.

Statement of data availability. Since the present study focuses on investigating how turbulence affects the preferential accumulation of finite-size particles in wall-bounded turbulence, discussions of the feedback effects, known as turbulence modulation, are excluded from the main text. During our simulations, we have gathered statistics of the mean flow velocity, mean velocity gradient, r.m.s. velocity and vorticity of each component, Reynolds stress and particle volume fraction. These statistics are phase-averaged in each x–z plane, i.e. only count the grid points located in the fluid phase, then time-averaged for over 30 large-eddy turnover times ($t^* = h/u_\tau$). To enhance the accessibility of our simulation data, these gathered flow statistics in each simulation are published as supplementary material. The corresponding results from the single-phase simulation are also provided, which serve as the baseline to quantify the effect of turbulence modulation.

This simulation was conducted in our previous study with domain size and grid resolution identical to those of the present work (Peng *et al.* 2019*b*).

Author ORCIDs.
Cheng Peng https://orcid.org/0000-0001-7652-3658;
Lian-Ping Wang https://orcid.org/0000-0003-4276-0051.

References

Berk, T. & Coletti, F. 2023 Dynamics and scaling of particle streaks in high-Reynolds-number turbulent boundary layers. *J. Fluid Mech.* **975**, A47.

Brändle de Motta, J.C., *et al.* 2019 Assessment of numerical methods for fully resolved simulations of particle-laden turbulent flows. *Comput. Fluids* **179**, 1–14.

Brenner, H. 1961 The slow motion of a sphere through a viscous fluid towards a plane surface. *Chem. Engng Sci.* **16** (3–4), 242–251.

Cisse, M., Homann, H. & Bec, J. 2013 Slipping motion of large neutrally buoyant particles in turbulence. *J. Fluid Mech.* **735**, R1.

Costa, P., Boersma, B.J., Westerweel, J. & Breugem, W.-P. 2015 Collision model for fully resolved simulations of flows laden with finite-size particles. *Phys. Rev.* E **92** (5), 053012.

Do-Quang, M., Amberg, G., Brethouwer, G. & Johansson, A.V. 2014 Simulation of finite-size fibers in turbulent channel flows. *Phys. Rev.* E **89** (1), 013006.

Eshghinejadfard, A., Zhao, L. & Thévenin, D. 2018 Lattice Boltzmann simulation of resolved oblate spheroids in wall turbulence. *J. Fluid Mech.* **849**, 510–540.

Fong, K.O., Amili, O. & Coletti, F. 2019 Velocity and spatial distribution of inertial particles in a turbulent channel flow. *J. Fluid Mech.* **872**, 367–406.

Gondret, P., Lance, M. & Petit, L. 2002 Bouncing motion of spherical particles in fluids. *Phys. Fluids* **14** (2), 643–652.

Ji, C., Munjiza, A., Avital, E., Xu, D. & Williams, J. 2014 Saltation of particles in turbulent channel flow. *Phys. Rev.* E **89** (5), 052202.

Joseph, G. 2003 Collisional dynamics of macroscopic particles in a viscous fluid. PhD thesis, California Institute of Technology.

Kidanemariam, A.G., Chan-Braun, C., Doychev, T. & Uhlmann, M. 2013 Direct numerical simulation of horizontal open channel flow with finite-size, heavy particles at low solid volume fraction. *New J. Phys.* **15** (2), 025031.

Kim, J., Moin, P. & Moser, R.D. 1987 Turbulence statistics in fully developed channel flow at low Reynolds number. *J. Fluid Mech.* **177**, 133–166.

Lucci, F., Ferrante, A. & Elghobashi, S. 2010 Modulation of isotropic turbulence by particles of Taylor length-scale size. *J. Fluid Mech.* **650**, 5–55.

Marchioli, C., Fantoni, M. & Soldati, A. 2010 Orientation, distribution, and deposition of elongated, inertial fibers in turbulent channel flow. *Phys. Fluids* **22** (3), 033301.

Marchioli, C. & Soldati, A. 2002 Mechanisms for particle transfer and segregation in a turbulent boundary layer. *J. Fluid Mech.* **468**, 283–315.

Maxey, M.R. 1987 The gravitational settling of aerosol particles in homogeneous turbulence and random flow fields. *J. Fluid Mech.* **174**, 441–465.

Moin, P. & Kim, J. 1982 Numerical investigation of turbulent channel flow. *J. Fluid Mech.* **118**, 341–377.

Moin, P. & Spalart, P.R. 1987 Contributions of numerical simulation data bases to the physics, modeling and measurement of turbulence. *Tech. Rep.* NASA-TM-100022.

Naso, A. & Prosperetti, A. 2010 The interaction between a solid particle and a turbulent flow. *New J. Phys.* **12** (3), 033040.

Niño, Y. & Garcia, M.H. 1996 Experiments on particle–turbulence interactions in the near-wall region of an open channel flow: implications for sediment transport. *J. Fluid Mech.* **326**, 285–319.

Pan, Y. & Banerjee, S. 1996 Numerical simulation of particle interactions with wall turbulence. *Phys. Fluids* **8** (10), 2733–2755.

Pedinotti, S., Mariotti, G. & Banerjee, S. 1992 Direct numerical simulation of particle behaviour in the wall region of turbulent flows in horizontal channels. *Intl J. Multiphase Flow* **18** (6), 927–941.

Peng, C. 2018 Study of turbulence modulation by finite-size solid particles with the lattice Boltzmann method. PhD thesis, University of Delaware.

PENG, C., AYALA, O.M., BRÄNDLE DE MOTTA, J.C. & WANG, L.-P. 2019*a* A comparative study of immersed boundary method and interpolated bounce-back scheme for no-slip boundary treatment in the lattice Boltzmann method. Part 2. Turbulent flows. *Comput. Fluids* **192**, 104251.

PENG, C., AYALA, O.M. & WANG, L.-P. 2019*b* A direct numerical investigation of two-way interactions in a particle-laden turbulent channel flow. *J. Fluid Mech.* **875**, 1096–1144.

PENG, C. & WANG, L.-P. 2019 Direct numerical simulations of turbulent pipe flow laden with finite-size neutrally buoyant particles at low flow Reynolds number. *Acta Mechanica* **230** (2), 517–539.

PESTANA, T., UHLMANN, M. & KAWAHARA, G. 2020 Can preferential concentration of finite-size particles in plane Couette turbulence be reproduced with the aid of equilibrium solutions? *Phys. Rev. Fluids* **5** (3), 034305.

PICANO, F., BREUGEM, W.-P. & BRANDT, L. 2015 Turbulent channel flow of dense suspensions of neutrally buoyant spheres. *J. Fluid Mech.* **764**, 463–487.

RASHIDI, M., HETSRONI, G. & BANERJEE, S. 1990 Particle-turbulence interaction in a boundary layer. *Intl J. Multiphase Flow* **16** (6), 935–949.

REEKS, M.W. 1983 The transport of discrete particles in inhomogeneous turbulence. *J. Aerosol. Sci.* **14** (6), 729–739.

RETTINGER, C. & RÜDE, U. 2022 An efficient four-way coupled lattice Boltzmann – discrete element method for fully resolved simulations of particle-laden flows. *J. Comput. Phys.* **453**, 110942.

SAFFMAN, P.G.T. 1965 The lift on a small sphere in a slow shear flow. *J. Fluid Mech.* **22** (2), 385–400.

SARDINA, G., SCHLATTER, P., BRANDT, L., PICANO, F. & CASCIOLA, C.M. 2012 Wall accumulation and spatial localization in particle-laden wall flows. *J. Fluid Mech.* **699**, 50–78.

SHAO, X., WU, T. & YU, Z. 2012 Fully resolved numerical simulation of particle-laden turbulent flow in a horizontal channel at a low Reynolds number. *J. Fluid Mech.* **693**, 319–344.

SMITH, C.R. & METZLER, S.P. 1983 The characteristics of low-speed streaks in the near-wall region of a turbulent boundary layer. *J. Fluid Mech.* **129**, 27–54.

SQUIRES, K.D. & EATON, J.K. 1990 Particle response and turbulence modification in isotropic turbulence. *Phys. Fluids* A **2** (7), 1191–1203.

SUZUKI, Y., IKENOYA, M. & KASAGI, N. 2000 Simultaneous measurement of fluid and dispersed phases in a particle-laden turbulent channel flow with the aid of 3-D PTV. *Exp. Fluids* **29** (Suppl 1), S185–S193.

VOTH, G.A. & SOLDATI, A. 2017 Anisotropic particles in turbulence. *Annu. Rev. Fluid Mech.* **49**, 249–276.

WANG, L.-P. & MAXEY, M.R. 1993 Settling velocity and concentration distribution of heavy particles in homogeneous isotropic turbulence. *J. Fluid Mech.* **256**, 27–68.

WANG, L.-P., PENG, C., GUO, Z. & YU, Z. 2016 Flow modulation by finite-size neutrally buoyant particles in a turbulent channel flow. *J. Fluids Engng* **138** (4), 041306.

XIA, Y., LIN, Z., PAN, D. & YU, Z. 2021 Turbulence modulation by finite-size heavy particles in a downward turbulent channel flow. *Phys. Fluids* **33** (6), 063321.

XIA, Y., XIONG, H., YU, Z. & ZHU, C. 2020 Effects of the collision model in interface-resolved simulations of particle-laden turbulent channel flows. *Phys. Fluids* **32** (10), 103303.

YANG, B., PENG, C., WANG, G. & WANG, L.-P. 2021 A direct numerical simulation study of flow modulation and turbulent sedimentation in particle-laden downward channel flows. *Phys. Fluids* **33** (9), 093306.

YOUSEFI, A., COSTA, P. & BRANDT, L. 2020 Single sediment dynamics in turbulent flow over a porous bed–insights from interface-resolved simulations. *J. Fluid Mech.* **893**, A24.

ZHU, C., YU, Z., PAN, D. & SHAO, X. 2020 Interface-resolved direct numerical simulations of the interactions between spheroidal particles and upward vertical turbulent channel flows. *J. Fluid Mech.* **891**, A6.